Preprints (www.preprints.org) | NOT PEER-REVIEWED | Posted: 16 November 2017 doi:10.20944/preprints201705.0014.v2

Peer-reviewed version available at *Remote Sens.* **2018**, *10*, 152; doi:10.3390/rs10010152

Article

Spectral and Spatial Cloud Detection Onboard for Hyperspectral Remote Sensing Image

Haoyang Li [1,*], Hong Zheng [1], Chuanzhao Han [2], Haibo Wang [3] and Min Miao [4]

[1] School of Automation Science and Electrical Engineering, Beihang University, No.37 Xueyuan Road, Beijing 100191, China; lhyang@buaa.edu.cn (H.L.); julyanna@vip.sina.com (H.Z.)
[2] China Academy of Space Technology, CASA, No.104 Youyi Road, Beijing 100094, China; hanchuanzhao_casc@foxmail.com(C.H.)
[3] China Centre for Resources Satellite Data and Application, No.5 Fengxian East Road, Beijing 100094, China; bo3861926@sina.com
[4] School of Mathmatics and System Science, Beihang University, No.37 Xueyuan Road, Beijing 100191, China; miaomin@buaa.edu.cn (M.M.)
* Correspondence: lhyang@buaa.edu.cn; Tel.: +86-10-8231-6970

Abstract: It is strongly desirable to accurately detect the clouds in hyperspectral images onboard before compression. However, conventional onboard cloud detection methods are not appropriate to all situation such as shadowed cloud or darken snow covered surfaces which are not identified properly in the NDSI test. In this paper, we propose a new spectral–spatial classification strategy to enhance the orbiting cloud screen performances obtained on hyperspectral images by integrating threshold exponential spectral angle map (TESAM), adaptive Markov random field (aMRF) and dynamic stochastic resonance (DSR). TESAM is performed to classify the cloud pixels coarsely based on spectral information. Then aMRF is performed to do optimal process by using spatial information, which improved the classification performance significantly. Some misclassification points still exist after aMRF processing because of the noisy data in the onboard environment. DSR is used to eliminate misclassification points in binary labeling image after aMRF. Taking level 0.5 data from hyperion as dataset, the average overall accuracy of the proposed algorithm is 96.28% after test. The method can provide cloud mask for the on-going EO-1 images and related satellites with the same spectral settings without manual intervention. The experiment indicate that the proposed method reveals better performance than the classical onboard cloud detection or current state-of-the-art hyperspectral classification methods.

Keywords: onboard cloud detecion; region of interest compression; themodynamic phase; spectral angle map; markov random field; dynamic stochastic resonance

1. Introduction

With the development of Hyperspectral remote sensing technology, hyperspectral imaging techniques have been widely used in many applications, including meteorological, earth observation, military affairs, etc. Meteorological satellite has obvious advantages in monitoring the continuity, spatiality and tendency of qualitative change of atmospheric environment. It provides important information for the omnidirectional monitoring of atmosphere state over the entire globe. Different from the concerns of meteorological satellites, earth observation satellites focus on the change of earth surface, city planning, geological prospecting, military reconnaissance and natural disaster. No matter what the application background is, most remote sensing images encompass the presence of clouds that, especially in the visible and infrared range, strongly affect the received electromagnetic radiation. Historically, clouds cover about 70% of the earth's surface[1] and play a dominant role in the energy and water cycle of our planet. But in this paper, earth's radiative budget or aerosol detection that influenced by clouds are not the main focus of our research. Typically, one hyperspectral image data has over 200 spectral bands, which presents a challenge for both data transmission and

© 2017 by the author(s). Distributed under a Creative Commons CC BY license.

Preprints (www.preprints.org) | NOT PEER-REVIEWED | Posted: 16 November 2017 doi:10.20944/preprints201705.0014.v2

Peer-reviewed version available at Remote Sens. 2018, 10, 152; doi:10.3390/rs10010152

storage[2]. Future earth exploration missions will face unprecedented data volumes. Data size have steadily increased due to improvements in detector, optics and onboard data handling technology. Compared with meteorological satellite, the data size of earth observation satellite is larger due to higher spatial resolution and revisiting frequency. Satellite-ground link (download speed) is more tense, which can be refered to the appendix for details. Given the fact that almost all these sensors have only limited memory capacity. And data transmission from the sensors to the ground become inevitable for the further data analysis[3]. The large data volumes affect mission requirements for the entire data handling chain, including onboard digitization, storage, downlink, ground processing, and distribution[4]. Bottlenecks along this path will constrain the instrument duty cycle, reducing science and application yield[5]. Depending on the application, clouds act as important information for meteorological research[6][7][8] or, as unwanted corruption for earth observation[9][10]. For the meteorological research users, data of image can be retained and transmitted to ground completely for further research. For non-meteorological research users, as a disturbance factor for earth exploration, cloud shaded the surface features who are the region of interest. As the invalid data, the data of cloud region can be discarded onboard directly. They are two kinds of onboard processing strategy.

Data compression is necessary for onboard processing. But lossy compression methods might not be suitable for hyperspectral images that are used in many accuracy demanding applications. Because the images are intended to be analyzed automatically by computers[11]. Bandwidth constraints have motivated new advanced lossless compression techniques such as the KLT algorithm[12][13][14] that have achieved compression rates of four or greater. Efforts to optimize lossless methods eventually face theoretical limits, but data size continues to increase. The challenge has driven research into other techniques that can further reduce data volumes while preserving science yield. For a specific application, it is very likely that only part region of the entire image carries the information of interest. Rather than compressing the entire image, sometimes it just needs to compress region of interest (ROI) of the image[15]. Compression methods will benefit significantly from simply not compressing those invalid data regions for the sake of a higher compression ratio. Cloud region is regarded as arbitrary shape of region. The ROI map will be generated to describe the shape of cloud region. And ROI map can be encoded by using ARLE[16] algorithm. The ROI map with 400×256 pixels can be maximally compressed into 3200bit whose compression ratio is 1:256. It is 0.002 % of the original data size, which is fairly small. Excising data of cloud region before compression could significantly reduce data size. However, the community lacks an accurate algorithms of real-time cloud detection in instrument hardware.

Most onboard cloud detection methods are based on the radiometric features of clouds. The "classical" cloud detection applies threshold tests to spectral properties of the image[17][18]. Pixels whose values fall outside of valid ranges would be marked as clouds. For example, the algorithms that are corresponding to MODIS compares the selected visible and near-infrared (VNIR) and near-infrared (NIR) bands to predetermined thresholds and then aggregates the result in different combinations depending on land type[19][20][21][22]. These algorithms use a combination of 14 wavelengths and over than 40 tests. This underscores the intrinsic difficulty of constructing a universal and complete cloud screening procedure. We focus on the visible short wave infrared (VSWIR) electromagnetic spectrum from 0.4–2.5 μm. There are many studies of cloud detection in these wavelengths, and algorithms vary in their assumptions and complexity. Of direct relevance to this work, onboard cloud detection has been demonstrated onboard the EO-1 spacecraft[23]. EO-1 cloud detection uses the solar zenith angle to compute the apparent top-of-atmosphere (TOA) reflectance. Then it applies a branching sequence of threshold tests based on carefully crafted spectral ratios to distinguish clouds and bright landforms such as snow, ice, and desert sand. The EO-1 cloud detection also acts as a data filtering step prior to onboard cryospheric and flood classification[24][25]. To our knowledge, it is the only previous case of cloud screening performed on orbit. Another kind of onboard cloud detection algorithms are mainly based on ACCA. They are used to give cloud-cover (CC) predictions to reduce

Preprints (www.preprints.org) | NOT PEER-REVIEWED | Posted: 16 November 2017 doi:10.20944/preprints201705.0014.v2

Peer-reviewed version available at Remote Sens. 2018, 10, 152; doi:10.3390/rs10010152

cloud contamination in acquired scenes[26][27][28]. These onboard cloud detecting methods are based on threshold decision tree (TDT) in general.

Even more complex algorithms which belongs to ground side are proposed. Some state-of-the-art cloud-screening techniques estimate the optical path from absorption features such as the oxygen A band, as in Gómez-Chova et al.[29] or Taylor et al[30]. Thermal infrared (TIR) channels can add brightness temperature information. Minnis et al. predict clear-sky brightness temperature values using ambient temperature and humidity and then excise pixels outside these intervals[31]. Texture cues can be utilized to recognize clouds by their high spatial heterogeneity[32]. Martins et al. demonstrated that a simple spatial analysis, i.e., the standard deviation of VNIR isotropic reflectance in a 3×3 pixel window, reliably discriminated clouds from aerosol plumes over ocean scenes[33]. Jin hu Bian et al. proposed spectral signature and spatio-temporal context method to distinguish snow from cloud[34]. Markov random field model was developed to segment hyperspectral image. Murtagh et al. represented spatial dependency by using a probabilistic Markov random field prior[35]. Haoyang Yu et al. proposed adaptive MRF method combined with SVM and achieve a good performance of classification of terrains[36]. Probabilistic model was another kind of cloud detection method. Gómez-Chova et al. use a gaussian mixture model to produce posterior probabilities. The Bayesian probabilistic model of Merchant et al. combines observational data with prior predictions from atmospheric forecasts, leading to true probabilistic predictions[37]. David R proposed the decision theoretic method (DTM) which was based on bayesian probabilistic model. The DTM achieved negligible false positives in cloud screening[38]. Recently, deep learning was widely used in classification of HSI. Li Wei et al. proposed hyperspectral image classification by using deep pixel-pair features[39]. Bin Pan et al. proposed a kind of vertex component analysis network which achieved better performance than some state-of-the-art method[40].

TDT method have more commission errors that are at high altitudes or at low solar illumination where snow was misclassified as clouds. The probabilistic model methods and the learning-based methods (such as neural network or supervised learning) have more omission errors. The omission errors were associated with optically thin clouds over underlying surface because of the incompleteness of training sample for this kind of cloud. Focusing on these problems, our method uses exponential spectral angle map, markov random field and dynamic stochastic resonance. The rest of this paper is organized as follows. Section 2 introduces the problems of onboard cloud detection method in detail. The proposed methodology for cloud detection is introduced in section 3. Performance evaluation for different operation scenarios by using a decade-year historical image archive of the "classic" hyperion spectrometer is given in section 4. Section 5 discusses the advantages, limitations and applicability of the proposed method. Section 6 presents the conclusions.

2. Related work

Current onboard cloud detection usually used the TDT method. The used bands of several typical TDT methods are shown in table 1. All of the three TDT methods use normalized difference snow index (NDSI). The NDSI test has difficulties with shadowed cloud or darken snow covered surfaces[41]. And it also has difficulties with the thin cloud. One scene is shown in figure 1. Since the complexity of various factors, it's hard to classify the cloud pixels completely only in spectral feature space, as shown in figure.1.(a) and (e). There are some omission errors (yellow region of figure.1.(e)) of cloud detection because the optical thickness of cloud is various. The three spectral curves in figure.1.(b) are sampled from three crosses marked in (a). The spectral difference between thin cloud and thick cloud is obvious especially in the bands of NIR. Near 1.25μm and 1.65μm, reflectance of the thin cloud is 62.2% and 14.8% of thick clouds respectively. It is because that spectrum of the thin cloud is heavily affected by underlying surface. Deviation of reflectance is such huge that one set of parameters is difficult to recognize various cloud completely. Commission errors also exist in cloud detection (e.g. the green region in figure.1.(e)) because spectral features of cloud and snow covered surfaces sometimes are similar under NDSI. Because there are different reflectance from various particles and

Preprints (www.preprints.org) | NOT PEER-REVIEWED | Posted: 16 November 2017 doi:10.20944/preprints201705.0014.v2

Peer-reviewed version available at Remote Sens. 2018, 10, 152; doi:10.3390/rs10010152

illumination. Figure.1.(c) shows two scenes that contain liquid cloud, mixed phase cloud, ice cloud and snow. Spectral normalization of the four materials are shown in figure.1.(d). In this scene, the black curve is TOA reflectance of a piece of thick ice cloud. The cyan curve is TOA reflectance of an unknown portion of the mixed phase cloud where the ice phase may be dominant. The red curve is TOA reflectance of a piece of liquid cloud. And the blue curve is the reflectance of snow. The normalized spectrum of the three cloud types has high consistency. The biggest difference of three curves is near 1.65μm. Liquid cloud has the highest reflectance near 1.65μm. But the reflectance of mixed phase cloud is lower and that of ice cloud is lowest. Envelope of spectrum of snow is different from spectrum of cloud near 1.03μm and 1.38μm, as shown in figure.1.(d). But reflectance of this snow region is almost the same as ice cloud near 0.56μm and 1.65μm. It happens to be the spectrum that are used by NDSI. For the two main existing problems of the cloud detection, figure.1.(f) symbolically illustrates that cloud pixels and ground pixels cannot be separated completely under TDT classifier because of the overlap of spectral features.

Table 1. Spectrum used by threshold methods and disadvantage

Method	The used spectrum	Disadvantage
ACCA [41]	0.45-0.52μm, 0.52-0.6μm, 0.62-0.69μm, 0.76-0.96μm, 1.04-1.25μm, **1.55-1.75μm**	It use NDSI=($\rho_{.56}$-$\rho_{1.65}$)/($\rho_{.56}$+$\rho_{1.65}$) index which contains spectral bands near 1.65μm to discriminate snow and cloud. But sometimes the snow covered surfaces and clouds cannot be classified clearly under NDSI because the reflectance features of cloud and snow particles sometimes are similar in particular spectrum.
HCC [23]	0.55μm, 0.66μm, 0.86μm, 1.25μm, 1.38μm, **1.65μm**	
DCC-ASE [24]	0.43μm, 0.56μm, 0.66μm, 0.86μm, 1.25μm, 1.38μm, **1.65μm**	

The influence of clouds on solar radiation is due to reflectance, absorption and scattering of the radiation by cloud particles. It depends strongly on the dimensions, opacity, thickness and composition of the clouds. There are different types of clouds with different dimensions, opacity and properties depending on several parameters, resulting to a different effect on solar radiation. The clouds are divided into ten types as seen in table 2. Ice crystals and water drops have a different impact at the absorption and scattering of solar radiation especially in SWIR. According to statistics from 184 scenes of Hyperion level 0.5 data, the solar reflectance of 10 cloud types and different ground types can be seen in electromagnetic spectrum from 0.4-2.5um, as shown in figure.2. Different clouds may have the different amplitude of reflectance. After normalization, the envelope of the spectral curve are roughly the same, as shown in figure.2.(a). However, different surface features have different spectral reflectance, as shown in figure.2.(b). In this paper, we mainly focus on how to detect cloud pixels instead of recognizing different types of cloud.

The pure threshold method is a simple, efficient, and practical approach for cloud detection, but its sensitivity to the background and the cloud condition, which makes it impractical for general use[42]. Comparing with threshold method, spectral angle map (SAM) have a better cloud detecting performance because of taking advantage of the more spectral information. In this paper, we demonstrate a cloud-detecting algorithm which mainly uses threshold exponential spectral angle map (TESAM), adaptive markov random field (aMRF) and dynamic stochastic resonance (DSR). In order to get an accurate cloud cover region, we presented TESAM-aMRF-DSR method for cloud detecting. The following sections describe the algorithm's theoretical method.

Preprints (www.preprints.org) | NOT PEER-REVIEWED | Posted: 16 November 2017 doi:10.20944/preprints201705.0014.v2

Peer-reviewed version available at Remote Sens. 2018, 10, 152; doi:10.3390/rs10010152

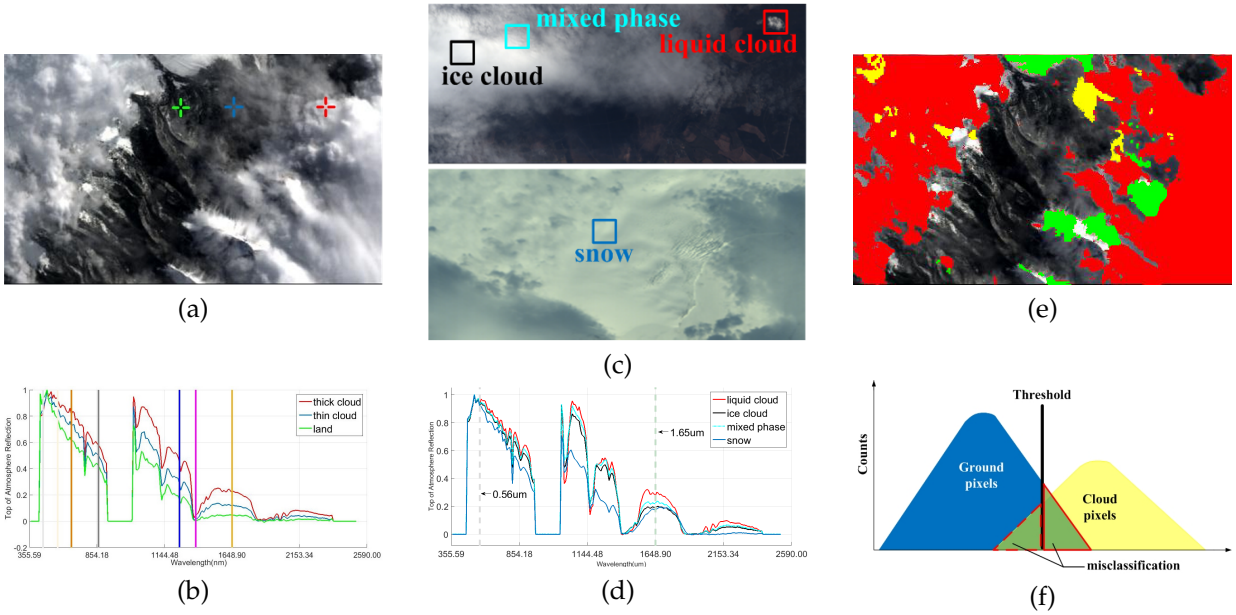

Figure 1. Cloud detection result under TDT method. (a) Original image; (b) spectrum of thick cloud, thin cloud and surface features that are sampled from red, blue and green cross in (a); (c) Two scenes that contain liquid cloud, mixed phase cloud, ice cloud and snow are labeled by box; (d) spectrum of liquid cloud, mixed phase cloud, ice cloud and snow that are sampled from the region in the boxes of (c) correspondingly; (e) cloud detection result under TDT method (red denotes extracted correct cloud region, yellow denotes omission errors and green denotes commission errors) (f) Diagrammatic sketch of misclassification between ground and cloud pixels under TDT method.

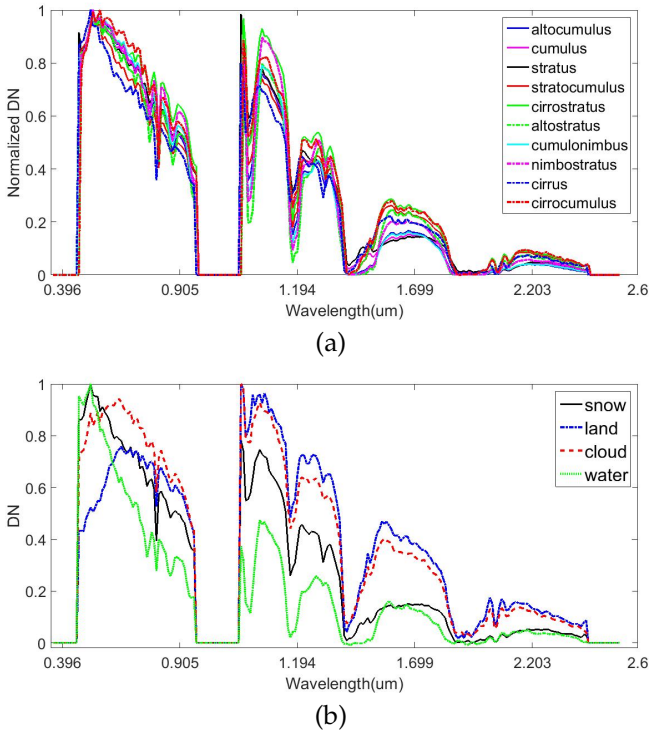

Figure 2. Spectral curve statistics of cloud and ground reflectance. (a) Normalized spectral reflectance curve of different cloud types. (b) Normalized spectral reflectance curve of different materials.

Preprints (www.preprints.org) | NOT PEER-REVIEWED | Posted: 16 November 2017 doi:10.20944/preprints201705.0014.v2

Peer-reviewed version available at Remote Sens. 2018, 10, 152; doi:10.3390/rs10010152

Table 2. Characteristic of 10 types of cloud

themodynamic phase	cloud type	characteristic
Water cloud	Cumulus (Cu) Stratocumulus (Sc) Stratus (St) Cumulonimbus (Cb)	They are composed of water droplets.
Mixed phase cloud	Altocumulus (Ac) Altostratus (As) Nimbostratus (Ns)	They are composed primarily of water droplets; however, they can also be composed of ice crystals when temperatures are low enough.
Ice cloud	Cirrus (Ci) Cirrocumulus (Cc) Cirrostratus (Cs)	They are typically thin and white in appearance, but can appear in a magnificent array of colors when the sun is low on the horizon.

3. Proposed method

For the questions mentioned above, a new method was proposed. The general framework of the proposed methods is shown in figure.3.(a). The hyperspectral images are processed by TESAM. After obtaining the basic classification result from TESAM, aMRF processes based on it. Then the output of aMRF is the input of DSR. Finaly, the reference spectrum is refreshed based on the final classification. The flowchart of each stage is as following. TESAM is divided into two parts, TDT and ESAM. The uncertainty of angle of illumination and thermodynamic phase will leads to misclassification for TDT methods. Some snow covered ground and the ground whose spectrum overlaps with the spectrum of cloud are misclassified as cloud under TDT, as shown in figure.3.(b). But TDT method can obtain the preliminary acreage of cloud region. The ESAM can be a better calculation of the distance between two spectral vectors because it is robust to illumination variations. And the ESAM represents the composition of the spectral reflectance in the form of vector. It calculates the cosine angle between target spectrum and reference spectrum. Then histogram can be obtained from cosine angles. The preliminary acreage of cloud and the histogram jointly decide whether the pixel is cloudy or not. A distinctive feature of cloudy pixel is that the non-absorbing 0.44μm-0.96μm are sensitive to cloud optical thickness (COT) and most of the absorbing channels within 1.03μm-2.4μm are sensitive to cloud effective particle radius (CER). TESAM tooks advantages of thses bands. The misclassification reduces under TESAM. The aMRF describes the interaction between adjacent pixels by using energy index. The energy is determined by spectral dimension and spatial dimension jointly. Relationship of eight adjacent pixels in spatial dimension is taken into consideration. The aMRF chooses 1.38μm$\sim$1.39μm and 1.46μm$\sim$1.55μm, which mainly takes advantage of vapor reflectance bands. Although the spectrums of some thin cloud pixels and some dark cloud pixels deviate from range of threshold a lot, classification result of the aMRF would not have wide range of errors. After iterative processing by using minimum energy, the omission errors and commission errors both reduce. The aMRF plays a role of optimization. But the onboard processing data belongs to level-0.5. This indicates that the images are without radiometric calibration. Therefore, during the process of aMRF, some points whose energy is mutated would be misclassified, as shown in the lower right corner of figure.3.(b). These misclassified points are seemed as noisy points in binary cloud mask. DSR eliminates these noisy points by using double-well model. DSR makes the isolated noisy points a transition from one state to another by combining with the attributes of adjacent pixels. It plays a role of refinement.

Preprints (www.preprints.org) | NOT PEER-REVIEWED | Posted: 16 November 2017 doi:10.20944/preprints201705.0014.v2

Peer-reviewed version available at Remote Sens. 2018, 10, 152; doi:10.3390/rs10010152

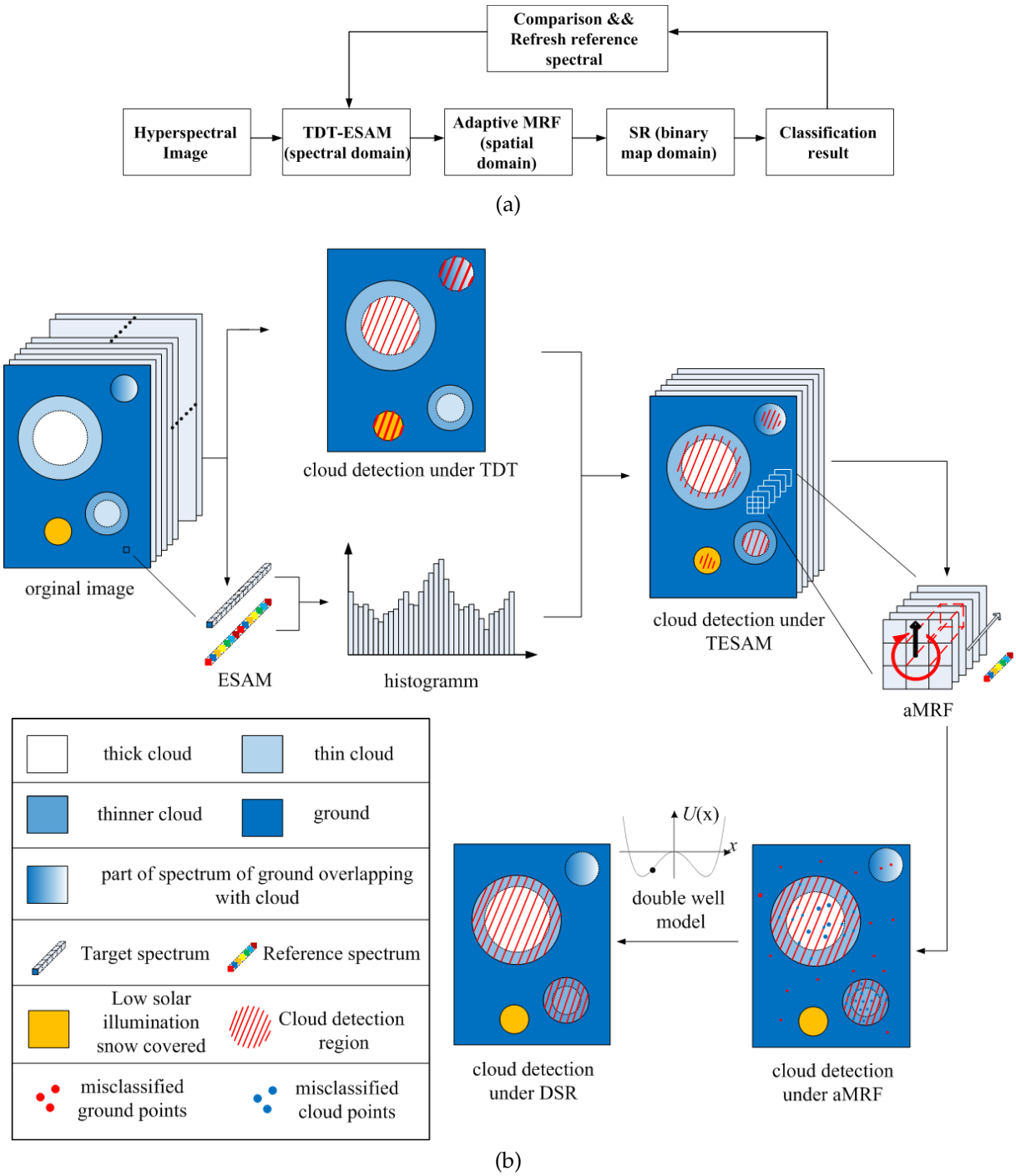

Figure 3. General framework and flowchart of the proposed methods.

Preprints (www.preprints.org) | NOT PEER-REVIEWED | Posted: 16 November 2017 doi:10.20944/preprints201705.0014.v2

Peer-reviewed version available at Remote Sens. 2018, 10, 152; doi:10.3390/rs10010152

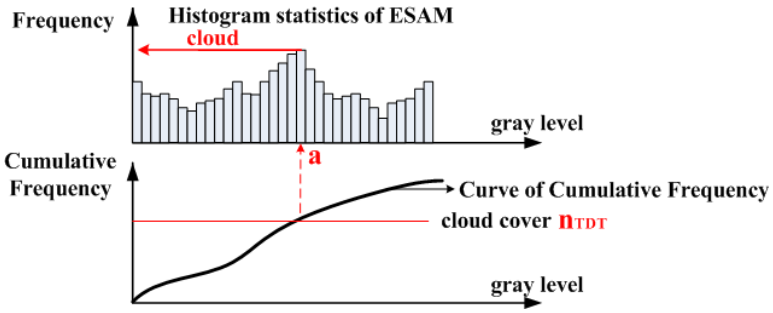

Figure 4. combination of ESAM with TDT.

3.1. T-ESAM

SAM calculates the angle θ(x,y), where x and y are N-dimensional spectral, $\{x_i\}_{i=1}^N$ and $\{y_i\}_{i=1}^N$, respectively,

$$\theta(x,y) = arccos(\frac{\langle \mathbf{x},\mathbf{y}\rangle}{\|\mathbf{x}\| \cdot \|\mathbf{y}\|}),\ 0 \le \theta \le \frac{\pi}{2} \tag{1}$$

where $\langle \mathbf{x},\mathbf{y}\rangle$ is the scalar product between $\mathbf{x}$ and $\mathbf{y}$

$$\langle \mathbf{x},\mathbf{y}\rangle = \sum_{i=1}^{N} x_i \cdot y_i \tag{2}$$

and $||\cdot||$ means the Euclidean norm, i.e, $\left\|\mathbf{x}^2\right\| = \langle \mathbf{x},\mathbf{x}\rangle$. The $\mathbf{x}$ means the target spectral vector. And $\mathbf{y}$ means the referenced spectral vector.

TDT methods for cloud detection onboard such as ACCA algorithm [26] for multispectral and HCC algorithm [23] for hyperspectral appear to be good discriminators for most of the circumstance. The performance of these cloud detection algorithms are not good enough (75% of the ACCA scores were within 10% of the actual cloud cover content)[26]. This situation can be improved under SAM. And we have encapsulated the SAM metric inside an exponential function to produce ESAM function which is a positive semi-definite function. The ESAM function is defined as

$$ESAM(x,y) = exp(-\theta(\mathbf{x},\mathbf{y}) \cdot k) \tag{3}$$

where k is the gain parameters. The resolution of ESAM is getting lower when k is getting lower. Generally, k is set as 0.5 (between 0 to 1). ESAM amplifies the angular distance between two vectors.

After the 3-D original hyperspectral image $\mathbf{I}_{[\mathbf{L},\mathbf{W},\mathbf{H}]}$ processing by ESAM, we can obtain a 2-D computing result. The lowest value indicates most similar spectrum. These data are most likely cloud region if there are clouds in the image. Simultaneously, threshold algorithms also have detected the result of cloud region. Then we can obtain the classifier by combining ESAM with TDT, as shown in figure.4. Through TDT method, we could obtain the mumber of cloud pixels n_{TDT} which is the red solid line. The curve of cumulative frequency can be drawn when the histogram of an image has been calculated. The intersection between n_{TDT} and curve of cumulative frequency locates the threshold value "a" of the histogram of ESAM.

$$\sum_{i=g(min)}^{g(n)} histogram(ESAM(I,y) = i) \le n_{TDT} \tag{4}$$

$$\sum_{i=g(min)}^{g(n+1)} histogram(ESAM(I,y) = i) \ge n_{TDT} \tag{5}$$

Preprints (www.preprints.org) | NOT PEER-REVIEWED | Posted: 16 November 2017 doi:10.20944/preprints201705.0014.v2

Peer-reviewed version available at Remote Sens. 2018, 10, 152; doi:10.3390/rs10010152

where "histogram(ESAM(I,y)=i)" means histogram statistics of the ESAM results between hyperspectral image and referenced spectrum that equals to “i”. The **g(min)** and **g(n)** indicate the frequencies corresponding to gray level minimum and gray level **n** respectively. Then we could obtain a classifier parameter **g(n)** which detects the cloud region coarsely when **g(n)** satisfies equation (4) and equation (5) at the same time. The cloud detection coarse classifier is defined as

$$f(x) = \begin{cases} c_1, if\ ESAM(x,y) < g(n) \\ c_2, if\ ESAM(x,y) \geq g(n) \end{cases} \tag{6}$$

The observed spectrum of instrument data forms a vector x with multiple spectral channels per pixel. The cloud-screen decision maps these pixel brightness values to a binary classification **c**=**f(x)** : $\mathbf{R}^d \rightarrow \{\mathbf{c}_1, \mathbf{c}_2\}$, where c_1 represents that there is a cloud present and c_2 represents the event that clear sky is observed. Classifier f(x) detects the cloud coarsely.

Algorithm 1 TDT assisted ESAM

Input: the remote sensing image data I with K pixels, each pixel is N-dimentional spectral vectors **X**=$\{x_i\}_{i=1}^N$, the referenced spectrum **Y**=$\{y_i\}_{i=1}^N$

Output: the class labels map **M**

step1:
  for k=1 to K do
    E_I=$\psi(X_K, Y)$ (ψ computes the exponential spectral angle according to Equations(1)-(3)).
  end
  for k=1 to K do
    n_{TA}_I=$\phi(X_k)$ (ϕ computes the number of cloud pixels according to TDT)
  end
step2:
  Computes the histogram of E_I
step3:
  for k=1 to n do
    $g(n)_I = \Omega(E_I)$ (Ω computes the threshold for ESAM according to Equations(4)-(5))
  end
Step4:
  for k=1 to K do
    $f(x)_I$=Y(E_I) (Y determine the binary class label according to Equations(6))
  end

3.2. aMRF model

The MRF model provide an accurate feature representation of pixels and their neighborhoods. The basic principle of aMRF is to spatial correlation information into the posterior probability of the spectral features. Based on the maximum posterior probability principle, the classic MRF model can be expressed as follows:

$$p(x_i) = -\frac{1}{2} ln|\Sigma_K| - \frac{1}{2}(x_i - m_k)^T \Sigma_K^{-1}(x_i - m_k) - \gamma_i \sum_{\alpha i}[1 - \delta(\psi_{ki}, \psi_{\varepsilon i})] \tag{7}$$

Where m_k and Σ_K are the mean vector and covariance matrix of class k respectively. And the neighborhood and class of pixel i are represented by ε_i and ψ_k respectively. Equation (6) separate the pixels of remote sensing image into 2 classes, ground pixels and cloud pixels. The parameter γ_i is the weight coefficient, which is used to control the influence of the spatial term.

Preprints (www.preprints.org) | NOT PEER-REVIEWED | Posted: 16 November 2017 doi:10.20944/preprints201705.0014.v2

Peer-reviewed version available at Remote Sens. 2018, 10, 152; doi:10.3390/rs10010152

To obtain the local spatial weight coefficients γ_i, Haoyang Yu[43] etc. used the noise-adjusted principal components (NAPC) transform to obtain the first principal component to calculate the γ_i,

$$\gamma_i = \gamma_0 \cdot RHI_i = \gamma_0 \cdot \frac{var_k}{var_i} \tag{8}$$

where var_k represents the class-decision variance of the neighborhood of pixel i as determined by majority voting rules and var_i is the local variance of pixel i [44]. When RHI_i is high, it can be concluded that pixel i is located in a homogeneous region. By contrast, pixel i is on a boundary when RHI_i is low. The local spatial weight coefficient when var_i=var_k; usually, γ_0= 1.

According to Equation (7), the aMRF model can be devided into two components: the energy of spectral term a_i(k) and the energy of spatial term b_i(k). Thus, Equation (7) can be represented in the form

$$p(x_i) = a_i(k) + \gamma_i \cdot b_i(k) \tag{9}$$

where $\delta(\psi_{ki}, \psi_{\varepsilon i})$ is the Kronecker delta function, defined as

$$\delta(\psi_{ki}, \psi_{\varepsilon i}) = \begin{cases} 1, \psi_{ki} = \psi_{\varepsilon i} \\ 0, \psi_{ki} \neq \psi_{\varepsilon i} \end{cases} \tag{10}$$

The pseudocode for the TESAM algorithm combined with the aMRF algorithm, abbreviated as TESAM-aMRF, is shown in Algorithm 2.

Algorithm 2 TESAM-aMRF

Input: the remote sensing image data **I** with K pixels, each pixel is n-dimentional spectral vectors **X** = $\{x_i\}_{i=1}^n$, the referenced spectrum **Y**=$\{y_i\}_{i=1}^n$, the class labels map **M**.

Output: the class labels map **M′**

step1: Computes the labels map **M** (results of TDT-ESAM) according to Algorithm 1;
step2: Computes the m_k and Σ_k according to class labels map and **I**; (k=2);
step3: Computes the $p(x_i)$ according to Equations (7)-(10), where computing the Equations (10) with class labels map;
step4: Refresh the class labels map **M** with minimal class of $p(x_i)$;
step5: Iterate the procedure of step2-step4;

3.3. DSR model

The DSR model here is used to denoise the cloud mask. In analogy to Benzi's double-well model, the binary image pixel value is treated as the position of a particle in the double well. Addition of stochastic energy effects its transition to the strong signal state, just as a particle makes a transition from one well to another. Such a change of state of pixel under noise can be modelled by Brownian motion of a particle placed in a double-well potential system shown in figure.5. The particle A is located in the left well. The state of particle A may or may not turn over in the double well after giving a sochastic energy to A. The location of particle A may be at ponit B if it does not turn over. And the location may be at point C if it turns over. The left and the right well represents black and white pixel of binary cloud mask respectively.

A classic 1D nonlinear dynamic system that exhibits SR is modelled with the help of the Langevin equation of motion is given below

$$m \cdot \frac{d^2x(t)}{dt^2} + \gamma \cdot \frac{dx(t)}{dt} = -\frac{dU(x)}{dx} + \sqrt{D} \cdot \xi(t) \tag{11}$$

Preprints (www.preprints.org) | NOT PEER-REVIEWED | Posted: 16 November 2017 doi:10.20944/preprints201705.0014.v2

Peer-reviewed version available at Remote Sens. 2018, 10, 152; doi:10.3390/rs10010152

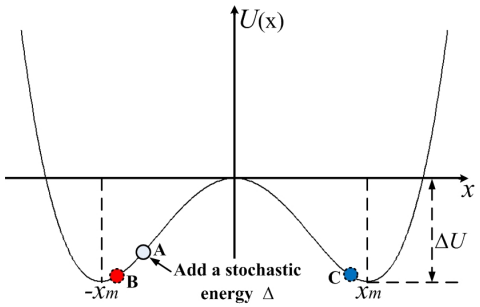

Figure 5. SR in double-well potential valley.

This equation describes the motion of a particle of mass m moving in the presence of friction, γ. The restoring force is expressed as the gradient of some bistable potential function U(x). In addition, there is an additive stochastic force $\xi(t)$ of intensity D.

If the system is heavily damped, the inertial $m\frac{d^2x(t)}{dt^2}$ term can be neglected. Rescaling the system in (11) with the damping term γ gives the stochastic overdamped Duffing equation, which is frequently used to model non-equilibrium critical phenomena as given in (12)

$$\frac{dx(t)}{dt} = -\frac{dU(x)}{dx} + \sqrt{D}\cdot\xi(t) \tag{12}$$

where U(x) is a bistable quartic potential given in

$$U(x) = -a\cdot\frac{x^2}{2} + b\cdot\frac{x^4}{4} \tag{13}$$

Here, a and b are positive bistable double-well parameters. The double-well system is stable at $x_m = \pm\sqrt{\frac{a}{b}}$ separated by a barrier of height $\Delta U = \frac{a^2}{4b}$ when $\xi(t)$ is zero. The Langevin equation describes the motion of particle in a general double-well.

Algorithm 3 aMRF-DSR

Input: the class labels $\mathbf{M}'$
Output: the class labels $\mathbf{M}_{final}$
step1:
for k=1 to K do
$C_k = \zeta$ ($\mathbf{M}'$(k)=**cloud**), $G_k = \zeta$ ($\mathbf{M}'$(k)=**ground**) (ζ computes the pixel number of 8-neighborhood around pixel k that belongs to ground and cloud respectively);
compare C_k and G_k , designating the number of bigger one to $\xi(t)$;
Refresh x according to Equations (12)-(13);
end
step2: Refresh $\mathbf{M}'$
step3: Iterate the procedure of step1-step2;

4. Method Feasibility Validation

4.1. Dataset

In this section, we evaluate the performance of the proposed algorithms by using the widely used hyperspectral data from hyperion sensor of EO-1. The data used in onboard processing is level 0.5. And they are downloaded from USGS website. Terrains of the dataset contain city, ocean, forest, mountain

Preprints (www.preprints.org) | NOT PEER-REVIEWED | Posted: 16 November 2017 doi:10.20944/preprints201705.0014.v2

Peer-reviewed version available at Remote Sens. 2018, 10, 152; doi:10.3390/rs10010152

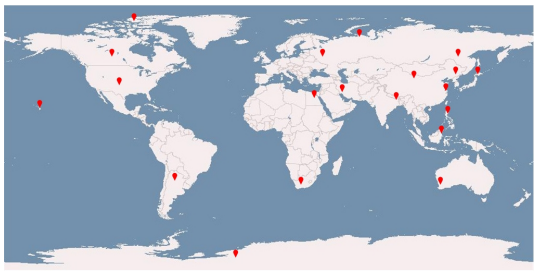

(a)

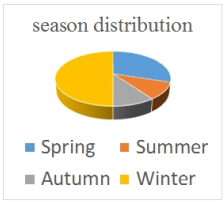

(b)

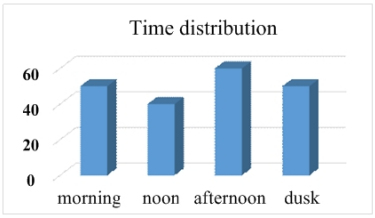

(c)

	Ordinary Terrain		Special Terrain	
Terrain	City	Forest	Snow	Cryosphere
number	18	17	28	21
Terrain	Field	Mountain	Desert	Ocean
number	29	36	17	18

(d)

Figure 6. Test dataset description. (a) Geographical distribution of the selected scene; (b) Season distribution of the selected scene; (c) Time distribution of the selected scene; (d) Scene number of each terrain.

range, desert, snow and cryosphere. The span of time contains spring, summer, autumn, winter, morning, noon and dusk of recent decade year. The span of latitude contains tropical, subtropical, temperate, frigid and polar zone. Geographical distribution of the selected scenes is spread all over the world. Season distribution is at all seasons but mainly focusing on winter. Statistics of test dataset is shown in figure.6.

In meteorological research, clouds are labeled pixel by pixel through particle scattering models. The single scattering properties of liquid water clouds are calculated from Mie theory[48] and are integrated over a Modified Gamma droplet size distribution. The single scattering properties of ice clouds are obtained from Yang et al[49]. Computed single scattering properties (single scattering albedo, asymmetry parameter, extinction efficiency, phase function) for both ice and liquid water clouds are stored in the LUT. However, for earth observed satellite, resolution is higher than meteorological satellite. Particle scattering models can't guarantee that each cloud pixel has been labeled just through the spectrum. The groundtruth of cloud is that manual label uses Visual Cloud-Cover Assessment method (VCCA). This method was used as a measure of the true cloud cover in the scene. The magic wand and freehand lasso tools of Photoshop were used to isolate clouds. The wand employs a seed-fill threshold algorithm to compute regions of brightness similarity based on a mouse click of a single pixel. The algorithm compares the selected pixel's brightness values to all other pixels and retains those within a selectable tolerance threshold. Additional cloud pixels are added by using the wand repeatedly until the cumulative selection of visible clouds had essentially zero possibility of VCCA omission errors. Snowfields and other unwanted bright features were then manually subtracted using the lasso tool to reduce VCCA commission errors. All these works were done by well-trained professional persons. After the VCCA scores were established, the result was a binary cloud mask that allowed a cloud cover percentage computation that served as the cloud "truth" for validating the accuracy of our proposed method. The uncertainty of manual labeling is the border of thin cloud and the cirrus which is floating on the snow especially in visible bands. Therefore, it is necessary to use infrared bands to label cloud pixels in assistant, but choosing which bands to separate cloud pixels from ground pixels maximally depends on surface features. It is another kind of uncertainty.

Preprints (www.preprints.org) | NOT PEER-REVIEWED | Posted: 16 November 2017 doi:10.20944/preprints201705.0014.v2

Peer-reviewed version available at Remote Sens. 2018, 10, 152; doi:10.3390/rs10010152

4.2. Accuracy Accessment

The following three different accuracies measures, which were the overall accuracy, precision and recall, were used to assess the accuracy of the algorithm results. Define the True Positive (TP) as the pixel-number of clouds correctly labeled as belonging to clouds in the algorithm, False Negatives (FN) as the pixel-number of clouds incorrectly labeled as belonging to non-cloud, and True Negatives (TN) as pixel-number of non-cloud which also labeled as belonging to non-cloud. The accuracy, precision and recall are then defined as

$$Recall = TP/(TP + FN) \tag{14}$$

$$Precision = TP/(TP + FP) \tag{15}$$

$$FPR = FP/(FP + TN) \tag{16}$$

In the cloud case, precision denotes the proportion of correctly detected cloud pixels in the cloud detection results, while recall is of all pixels that are actually clouds in the image, what fraction of them were detected as clouds. For precision and recall, they are better reflects the errors of cloud classification than overall accuracy.

4.3. Detection results

Figure.7 shows the cloud detection results for different terrains. Just by visually comparing the results with the false color composites, it is clear that the algorithm developed in this study achieves good performance in detecting the cloud pixels. Figure.7.(a) was a summer image acquired on 8^{th} August 2013 with cirrostratus over the desert. The detection result indicates that algorithm showed its strong ability in excluding the cloud from desert even if cloud is such thin that spectrum of cloud is mixed with spectrum of desert pixels. On the other hand figure.7.(b) was a winter image acquired on 3^{rd} June 2013 with dark stratus over the ocean and coast. Clouds contain water droplets that have the same materials of ocean in this season. However, water of the ocean is in liquid and water of clouds is in form of aerosol. Even if the spectrum of the same materials is different due to different forms or temperature. About 1.73% omission errors, the yellow region, which is different from manually labeled cloud mask exist on the border of thin cloud. Figure.7.(c) was a spring image acquired at noon on 22^{th} May 2012 with cumulus and stratocumulus around Himalaya mountains. And figure.7.(d) was a winter image acquired at dusk on 3^{rd} January 2007 with altocumulus over mountain with 0.62% omission errors. Comparing figure.7.(c) with figure.7.(d), cloud of the former seems lighter than the later due to smaller sun zenith angle. But both the two image have good cloud detection result even if the darker cloud can be also detected. Figure.7.(f) was a winter image acquired on 28^{th} March 2005 with cumulus over the city Haerbin. About 0.23% commission errors that both freezing river and city highlights are classified into cloud. About 0.16% omission errors exist in suspected cloud region. Figure.7.(e), figure.7.(i) and figure.7.(j) are both clouds over the snow or ice. Figure.7.(e) was an image acquired on 12^{th} May 2012 with stratocumulus over snowfield in the cryosphere. The cloud pixels, about 4.8% pixels of the whole image, are indistinguishable by naked eyes. These pixels are floating over the snow field. There are 0.41% commission errors when compared with manually labeled cloud mask. Figure.7.(i) was a spring image acquired on 17^{th} March 2007 with altostratus over mountain which is covered by snow. The edge of altostratus looks similar to ground because it doesn't have a clear outline in visible bands. Although there are 2.97% cloud pixels that are hard to be distinguished by eyes in visible bands, they were classified by the proposed method correctly. Figure.7.(j) was a spring image acquired on 28^{th} March 2005 with cumulus over the forest which is covered by some frozen lake. Most of the cumulus are floating on the ice. They have 0.21% omission errors.

4.4. Performance of Each Stage for the Cloud Detection

Figure.8 provides an illustration of the algorithm performance for the each processing stage. It depicts the cloud results for EO-1 Hyperion images from four different states. By visually comparing

Preprints (www.preprints.org) | NOT PEER-REVIEWED | Posted: 16 November 2017 doi:10.20944/preprints201705.0014.v2

Peer-reviewed version available at Remote Sens. 2018, 10, 152; doi:10.3390/rs10010152

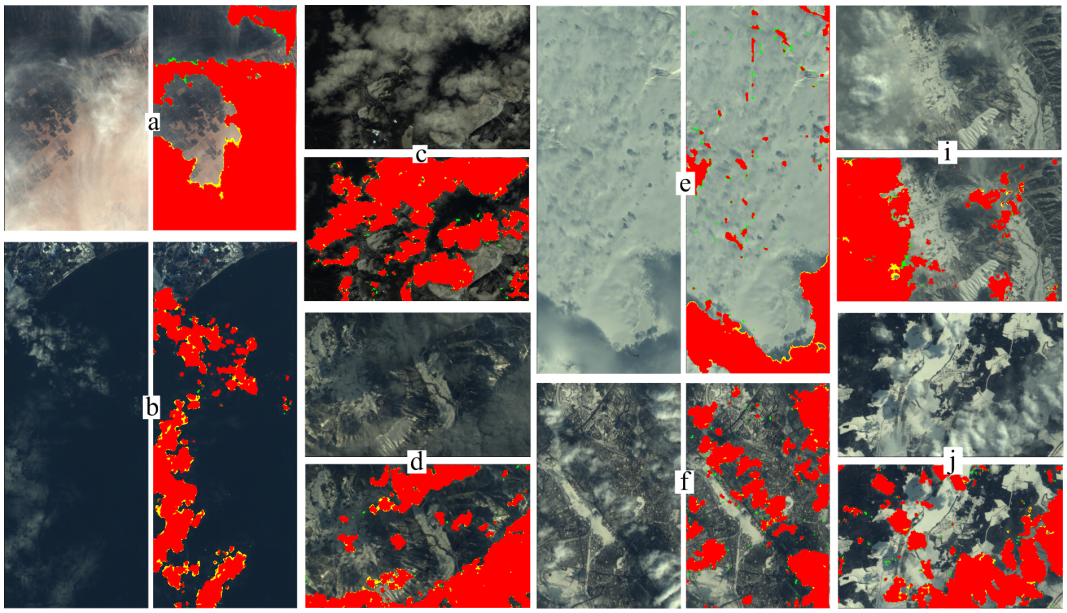

Figure 7. Cloud detection results for different kinds of ground. (a) Desert with thin cirrostratus and cloud detection result; (b) Ocean with dark stratus and cloud detection result; (c) Mount Qomolangma with stratocumulus and cloud detection result; (d) Mountain with dark altocumulus and cloud detection result; (e) Snow cover with straocumulus and cloud detection result; (f) Highlight city with frozen lake scene and cloud detection result; (i) Mountain with thin altostratus and cloud detection result; (j) Frozen field with cumulus and cloud detection result. (Red denotes extracted correct cloud regions (TP), yellow denotes missed cloud regions (omission errors/FN) and green denotes non-cloud regions misjudged as cloud regions (commission errors/FP))

the results with the false color composites, it is clear that there are FN classifications in light cloud region under TDT method because of the unsuitable and fixed parameters for various reflectance as shown in figure.8.(h). Contrarily, TESAM could classified the cloud regions that are misclassified under TDT method correctly, as shown in figure.8.(i). And under TESAM, the various reflectance didn't have much influence over cloud detection. Comparing with TDT, TESAM seems to be conservative, abstaining ambiguous classification to prevent mixture of heterogeneous spectrum for the aMRF procedure. The ambiguous classification is shown in the yellow circle of figure.8.(k). These region are not labeled as cloud under TESAM, as shown in figure.8.(l). After TESAM detecting, the cloud regions detected by TESAM work as a role of seed regions in the procedure of aMRF. By comparing yellow circles of figure.8.(d) and figure.8.(e), we can see that after aMRF detecting, some cloud regions grow more full. And TN regions have been recovered to ground pixels because the aMRF has fault-tolerant ability. The detailed iterative process of aMRF will be introduced later. But the spectrum of some individual pixels still has the strong similarity with cloud under the selected bands for aMRF. Therefore, even if considering the neighbors' contribution, the energy of these pixels under aMRF is still low. They were misclassified as cloud pixels. However, these pixels of cloud mask are seemed as noisy points for DSR. By comparing figure.8.(m) and figure.8.(n), DSR turned the binary properties of these noisy points over. The vertical line and some isolate pixels in figure.8.(m) have been eliminated after DSR processing, as shown in figure.8.(n).

The detailed example for iterative process of aMRF is shown in figure.9. The cloud regions that are detected by TDT method and TESAM are rather limited (0.02% and 0.12% of TP were within 18.3% of the actual cloud cover content). Only a few detected cloud pixels existed in the mask, as seen in figure.9.(a) and (b). The detection result of TESAM is treated as initial classification for aMRF. Comparing figure.9.(c-h), obviously, aMRF method have strong robustness if the spectrum of the initial seed region (seed region) is pure enough. The initial classification of each iteration is the result of the

Preprints (www.preprints.org) | NOT PEER-REVIEWED | Posted: 16 November 2017 doi:10.20944/preprints201705.0014.v2

Peer-reviewed version available at Remote Sens. 2018, 10, 152; doi:10.3390/rs10010152

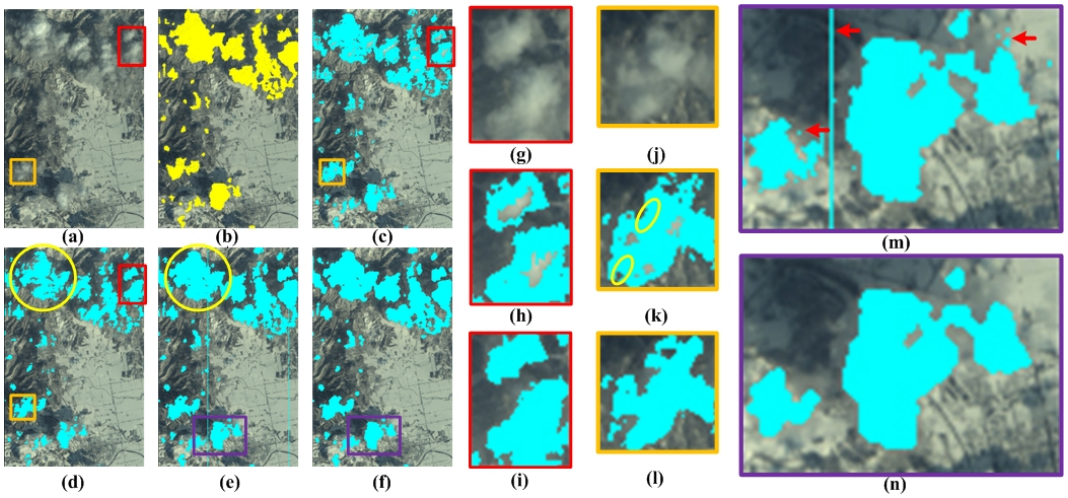

Figure 8. Comparison of cloud detection results. (a) A winter image acquired at 7 December 2013 with obvious clouds over the whole image; (b) Result of manually labeled image; (c) Cloud detection result by using TDT method; (d) Cloud detection result by using TESAM method; (e) Cloud detection based upon (d) by using aMRF method; (f) Cloud detection based upon (e) by using DSR; (g), (h) and (i) are origin picture, TDT labeled and TESAM labeled of cloud region respectively. (g), (h) and (i) are corresponding to the red box in (a), (c), (d) respectively; (j), (k) and (l) are corresponding to origin picture, TDT labeled and TESAM labeled of cloud region respectively. (j), (k) and (l) are corresponding to the orange box in (a), (c), (d); (m) is the result of aMRF processing, which is corresponding to purple box in (e); (n) is processed by DSR based on (e), which is corresponding to purple box in (f).

previous iteration. And after 8th iteration, classification has good agreement with the real cloud region. And this image tended to be convergent at the 16^{th} iteration.

Figure.10 shows comparison of cloud detection performance of some methods. The terrains from the first row to the last row are ocean, mountain, city, desert, ice and cryosphere. It can be observed that the proposed method produced the best precision ratio and recall ratio and its error was lower than that of the other methods. ACCA have high FN for ordinary terrain and high FP for special terrain due to lacking the thermal infrared band. HCC has difficulty in detecting thin or dark cloud. Decision Theoretical Method(DTM) classifies majority of thin clouds into ground. It is with high FP under DTM. The support vector machine adaptive markov random field (SVM-aMRF) and rolling guidance filter and vertex component analysis network(R-VCANet) have higher recall ratio and precision ratio than the previous two. But they still have some classification error for thin clouds

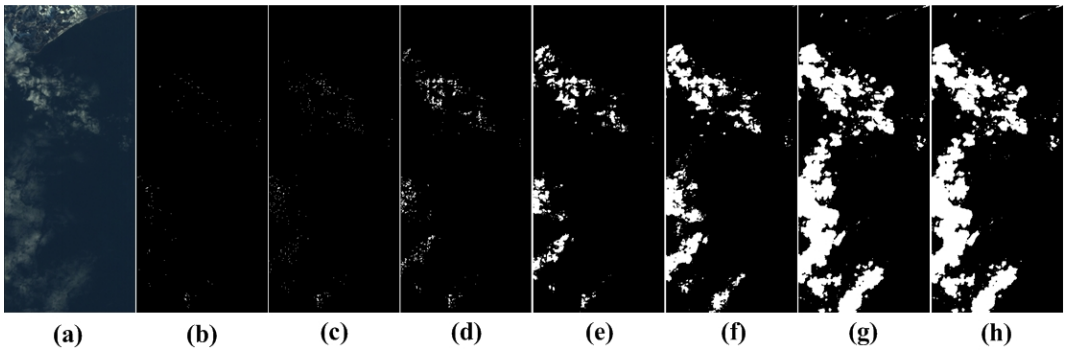

Figure 9. The detailed iteration result of aMRF. (a) Original image; (b) Classification result of TESAM; (c-h) The 1^{st}, 2^{nd}, 4^{th}, 8^{th}, 16^{th} and 30^{th} iteration result of aMRF respectively.

Preprints (www.preprints.org) | NOT PEER-REVIEWED | Posted: 16 November 2017 doi:10.20944/preprints201705.0014.v2

Peer-reviewed version available at Remote Sens. 2018, 10, 152; doi:10.3390/rs10010152

that mainly because thin clouds are mixed with other spectrum that can't be learned sufficiently. ROC curve and precision/recall curve can be seen in figure.11 and figure.12.

5. Discussions

5.1. The Effectiveness of Combining Threshold Decision Tree and Spectral Angle Map

Spectral Angle Map is widely used due to its simplicity and geometrical interpretability. SAM is invariant to (unknown) multiplicative scalings of spectra due to differences in illumination and angular orientation. One of the most important properties of the spectral angle distance is the invariance to multiplicative scaling. Due to the invariant nature of the angle among the linearly scaled variations, the spectral angle between two pixels is more sensitive to the pattern (shape) of the spectral signatures instead of absolute intensities. Traditional TDT methods sometimes overestimate or underestimate the cloud region because the fixed parameters were inappropriate to the variant illumination and angular orientation. In theory, TESAM method could reduce the misclassification error.

5.2. The Useness of Spatial Information for Cloud Detection

For still existing wrong classification pixels after TESAM, aMRF was used to synthesize all the spectral and spatial information into an energy index to find the class attribute at the regional scales. In general, it achieved the optimal status when the energy was stable, then the iteration procedure terminated. The aMRF mainly choose the bands of vapor reflection (1.38μm$\sim$1.39μm and 1.46μm$\sim$1.55μm). Spectrums of thin cloud pixels and dark cloud pixels deviate threshold a lot. But aMRF can recognize these cloud pixels again. The cloud mask resulted from aMRF contains noisy points because the data processed onboard belongs to level 0.5 that are not fully calibrated. The radiance and reflectance of values for SWIR bands of level 0.5 should be considered as pseudo-radiance and pseudo-reflectance. DSR can eliminate these noisy points of binary mask. It is a refinement process for cloud detection. Figure.12 shows that the over all accuracy of aMRF iteration results and DSR iteration results. We randomly selected parts of the dateset. Over all accuracy of each aMRF iteration results is shown in figure.12.(a). The 0^{th} iteration means over all accuracy after TESAM. During the aMRF iteration, the accuracy of each time increased more or less. The final performance of improved accuracy with aMRF iteration are not all the same because it mainly depends on cloud condition. The convergence criterion for aMRF iteration is that class attribute of 0.5% pixels won't change between two adjacent iterations. And the over all accuracy of each DSR iteration results is shown in figure.12.(b). The 0^{th} iteration means over all accuracy after aMRF. During the DSR iteration procedure, the accuracy of each time numerically increased little. But it eliminates many isolated noise-points, which are greatly beneficial to ROI compression. The convergence criterion for DSR iteration is that class attribute of 0.01% pixels won't change between two adjacent iterations.

5.3. Error Sources of the proposed Method

In brief, the cloud detection results indicated that the proposed method has a good performance for the detecting cloud in EO-1 images. However, two error sources which might influence the algorithm accuracy should also be pointed out. The first error source came from the way that the cloud region detected by TDT algorithm is bigger than actual size. That's probably because of unsuitable parameters. Correspondingly, TESAM will overestimate cloud areas because size of cloud region is decided by TDT and histogram of TESAM together. In this condition, it will increase FPR region of TESAM results. Because the impure cloud spectrum may lead to error classification of large area under aMRF. The second error is that the selected bands for aMRF may not be optimal for all kinds of surface features. In this case, the advantages of seed region are losed if the contribution from the weight of neighbor is not enough.

Preprints (www.preprints.org) | NOT PEER-REVIEWED | Posted: 16 November 2017 doi:10.20944/preprints201705.0014.v2

Peer-reviewed version available at Remote Sens. 2018, 10, 152; doi:10.3390/rs10010152

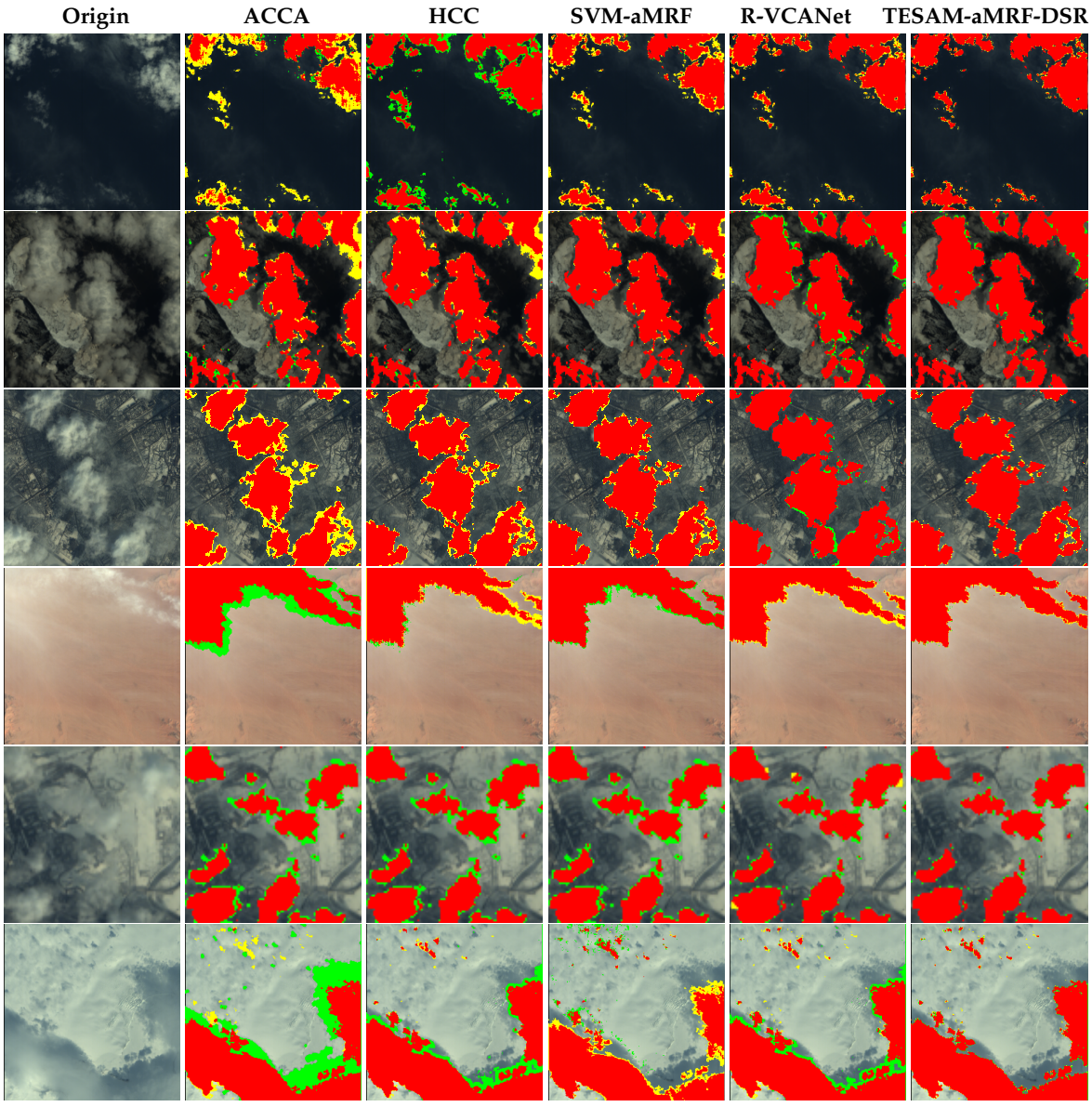

Figure 10. Cloud detection performance comparasion. (Red denotes extracted correct cloud regions (TP), yellow denotes missed cloud regions (omission error/FN) and green denotes non-cloud regions misjudged as cloud regions (commission error/FP))

Preprints (www.preprints.org) | NOT PEER-REVIEWED | Posted: 16 November 2017 doi:10.20944/preprints201705.0014.v2

Peer-reviewed version available at Remote Sens. 2018, 10, 152; doi:10.3390/rs10010152

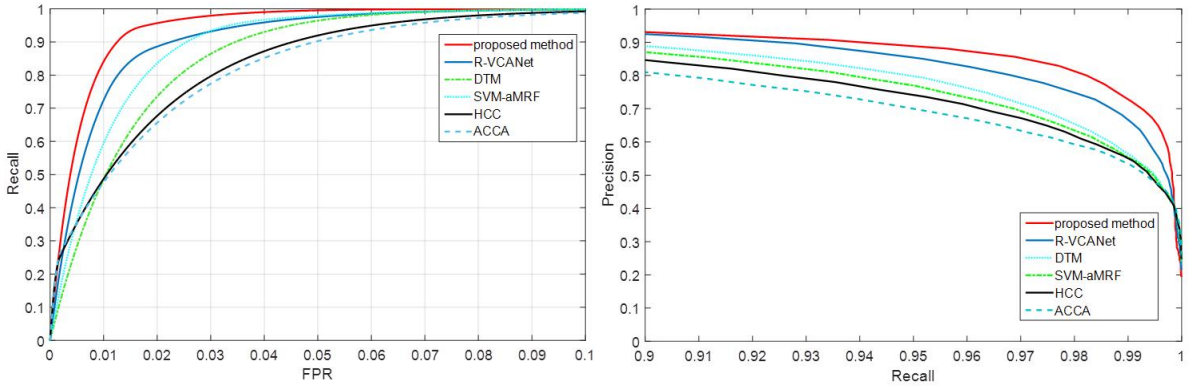

(a) (b)

Figure 11. Comparison of performance about the different algorithms. (a)ROC curve of cloud detection performance for each method. (b)Precision performance curve corresponding to Recall for each method.

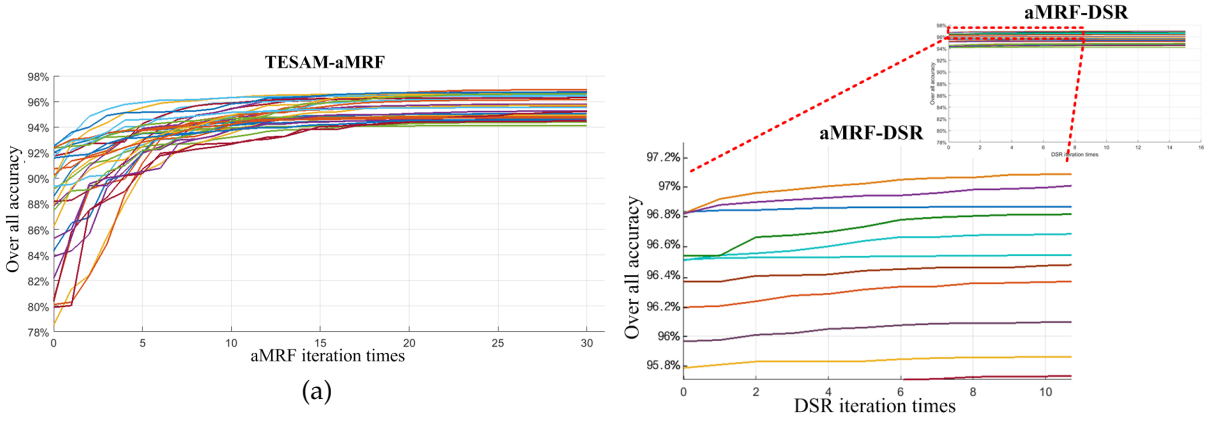

(a) (b)

Figure 12. Statistics of each iteration results of aMRF and DSR. (a)over all accuracy of aMRF iteration results. (b)over all accuracy of DSR iteration results.

Preprints (www.preprints.org) | NOT PEER-REVIEWED | Posted: 16 November 2017 doi:10.20944/preprints201705.0014.v2

Peer-reviewed version available at Remote Sens. 2018, 10, 152; doi:10.3390/rs10010152

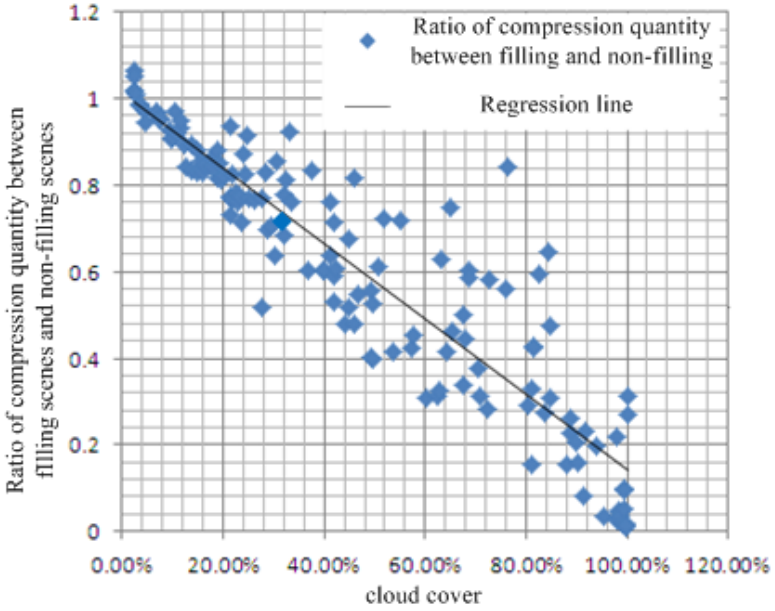

Figure 13. Statistics of cloud cover and ratio of compression quantity between filling and non-filling cloud regions.

5.4. Effect of compression based on cloud detection

The compression effect is worth mentioning. The cloud region is filled with special value after obtaining the cloud mask. Then the data of cloud region can be removed through compression. For a scene with 30.12% cloud cover rate of hyperion image, data size of the filled-value one is 71.27% of the original one that both of them have been processed by lossless compression. One hand, it is necessary to consider the difference of lossless compression ratio between ground and cloud. On the other hand, the non-filling cloud's contribution to compression is not as much as the filling cloud's. The statistics of cloud cover and ratio of compression quantity between filling and non-filling cloud regions is shown in figure 13. The regression line is shown that the ratio of compression quantity between filling and non-filling cloud regions is approximately proportional to the cloud cover ratio. The tendency is linear. And the closer to 1:1 they are, the better compression performance of filling-value it is. Some points that are higher than 1 means that the scene contains little thin cloud. Some points that are close to zero indicate that the scene is totally covered by cloud.

5.5. Applicability of the Developed Methods in the Feature

The proposed method is highly automatic and efficient when processing a tremendously large volume of imagery real-time. It can be easily implemented on a parallel processor, such as FPGA. The proposed method needs some external storage devices or the architectures such as ping-pong structure. Because it could restore data for supporting the use of spatial context. Moreover, classifiers instantiated in hardware logic typically have already achieved in the implementation of arccosine[45], exponentials[46][47] functions, and even floating-point operations, supporting many nonlinear classifiers and naive implementations of linear classifiers. Additionally, there are real-time requirements for processing procedure. Bandwidth of multi DDRs could satisfy Gb/s throughput of algorithm by using a small fixed number of arithmetic operations on locally available data. It also can be adapted for images acquired by similar satellite instruments, which have similar spectral bands and temporal resolutions. The method in this paper is general and efforts in the future will be put into the test for other regions with different environments.

Preprints (www.preprints.org) | NOT PEER-REVIEWED | Posted: 16 November 2017 doi:10.20944/preprints201705.0014.v2

Peer-reviewed version available at Remote Sens. 2018, 10, 152; doi:10.3390/rs10010152

6. Conclusions

The TESAM-aMFR-DSR is an innovative approach for onboard cloud detection. Different from classical hyperspectral cloud detection algorithm, the proposed method combines TDT with ESAM. As initial seed region of cloud for aMRF, it improves spectral purity. The aMRF method uses energy index by combining spectral features with spatial information. It is robust to the shadowed region of cloud area, the thin cloud and the misclassified ground pixels. There are noisy points that are misclassified during aMRF process because of not fully calibrated onboard processing data. Then DSR eliminated these noisy points by using double-well model. The cloud detecion results obtained in this study demonstrate the performance of the proposed method. The performances of this method are evaluated using EO-1/Hyperion images. Agreements were found between detection results and manually labeled image with the over all accuracy 96.28%. The spatial information can approximately exclude misclassified 8.35% cloud pixels from initial spectral tests. The ratio of compression quantity between filling scenes and non-filling scenes is approximately proportional to the cloud cover ratio. The tendency is linear. The filling cloud regions improve compression performance. In conclusion, the proposed method exhibited high accuracy for clouds recognition of EO-1 Hyperion images and was an improvement over the traditional spectral-based algorithms. The proposed method also can be adapted for images acquired by similar satellite instruments, which have similar spectral bands and temporal resolutions.

Acknowledgments: Project supported by the National Nature Science Foundation of China(No.60543006). The authors would like to thank the editor and reviewers for their instructive comments that helped to improve this manuscript. Besides, they would also like to thank the international scientific data service platform and the U.S. Geological Survey website

Author Contributions: Haoyang Li, Hong Zheng and Chuanzhao Han conceived of the study and designed the experiments; Haibo Wang and Min Miao took part in the research and analyzed the data; Haoyang Li wrote the main program and most of the paper.

Conflicts of Interest: The authors declare no conflict of interest.

Abbreviations

The following abbreviations are used in this manuscript:

Preprints (www.preprints.org) | NOT PEER-REVIEWED | Posted: 16 November 2017 doi:10.20944/preprints201705.0014.v2

Peer-reviewed version available at Remote Sens. 2018, 10, 152; doi:10.3390/rs10010152

ACCA	Automatic Cloud Cover Algorithm
aMRF	adaptive Markov Random Field
CC	Cloud Cover
DCC-ASE	Detection of Cryospheric Change Automonous Sciencecraft Experiment
DSR	Dynamic Source Resonance
DTM	Decision Theoretic Method
EO-1	Earth Observing-1
ESAM	Exponential Spectral Angle Map
FL	Fast Lossless
FN	False Negative
FP	False Positive
FPR	False Positive Rate
HCC	Hyperion Cloud Cover
HSI	Hyperspectral Image
LUT	Look Up Table
MRF	Markov Random Field
MODIS	Moderate-resolution Imaging Spectroradiometer
NAPC	Noise-adjusted Principle Components
NDSI	Normalized Difference Snow Index
NIR	Near Infrared
ROC	Receiver Operating Characteristic Curve
ROI	Region of Interest
R-VCANet	Rolling Guidance filter and Vertex Component Network
SAM	Spectral Angle Map
SVM	Support Vertor Machine
SVM-aMRF	Support Vector Machine adaptive Markov Random Field
TDT	Threshold Decision Tree
TESAM	Threshold assisted Exponential Spectral Angle Map
TIR	Thermal Infrared
TN	True Negative
TOA	Top of Atmosphere
TP	True Positive
USGS	United States Geological Survey
VNIR	Visible and Near Infrared
VSWIR	Visible and Short Wave Infrared

Appendix A

1. GEWEX, http://climserv.ipsl.polytechnique.fr/gewexca/
2. Hongda Shen; W. David Pan; Dongsheng Wu, Predictive lossess compression of regions of interest in hyperspectral images with no-data regions. IEEE Trans. Geosci. Remote Sens. **2016** *55*, 173-182.
3. Hongda Shen; W. David Pan; Dongsheng Wu, Predictive Lossless Compression of Regions of Interest in Hyperspectral Image Via Correntropy Criterion Based Least Mean Square Learning. In proceedings of IEEE International Conference on Image Processing, Phoenix, Arizona, USA, 25-28 Sept 2016.
4. L. Mandrake; C. Frankenberg; C. W. O'Dell; G. Osterman; P. Wennberg; D. Wunch, Semi-autonomous sounding selection for OCO-2. Atmosp. Meas. Tech. Discuss.**2013**, *6*, 5881–5922.
5. L. S. Chien; D.Mclaren; D. Tran; A. G. Davies; J. Doubleday; D. Mandl, Onboard product generation on earth observing one: A pathfinder for the proposed HyspIRI mission intelligent payload module. IEEE JSTARS. **2013**, *6*, 257–264.
6. Xiangxin Xu; Chunqiang Yuan; Xiaohui Liang; Xukun Shen, Rendering and Modeling of Stratus Cloud Using Weather Forecast Data. In Proc. Int. Conf. on Virtual Reality and Visualization, Fujian, China, 17-18 October 2015.

Preprints (www.preprints.org) | NOT PEER-REVIEWED | Posted: 16 November 2017 doi:10.20944/preprints201705.0014.v2

Peer-reviewed version available at Remote Sens. 2018, 10, 152; doi:10.3390/rs10010152

Table A1. Meteorological satellite VS Earth observation satellite

	Satellite	The used sensor	Image resolution	Data size	Download speed
Meteorological satellite	FY-3A	MERSI	1100m	4GB	93Mb/s
	Noaa18	AVHRR	1100m	/	138Mb/s
	GMS-5	VISSR	1250m	/	14Mb/s
	Meteosat	VISSR	1000m	/	3.2Mb/s
	Meteor-m2	KMSS	1000m	/	665kb/s
Earth observation satellite	EO-1	Hyperion	30m	/	120Mb/s
	NEMO(HRST)	AVIRIS	20m	227GB	150Mb/s
	QuickBird	QuickBird	0.6m	128GB	320Mb/s
	LANDSAT8	OLI/TIRS	15m	400GB	330Mb/s
	EROS B1	Panchromatic	0.82m	/	280Mb/s
	Resurs dk1	ESI	1m	768GB	330Mb/s

7. M. King, S. Platnick, W. Menzel, S. Ackerman, and P. Hubanks; M. Chodas, Spatial and temporal distribution of clouds observed by MODIS onboard the Terra and Aqua satellites. IEEE Trans. Geosci. Remote Sens. **2013**, *51*, 3826–3852.
8. E. Cadau; G. Laneve, Improved MSG-SEVIRI images cloud masking and evaluation of its impact on the fire detection methods. In Proc. IGARSS, Massachusetts, U.S.A., 6-11 July 2008.
9. Hongda Shen; W. David Pan; Yi Wang, A Novel Method for Lossless Compression of Arbitrarily Shaped Regions of Interest in Hyperspectral Imagery. In Proc. IEEE Southeast Con, Florida, USA, 9 - 12 April 2015.
10. M. Mercury; R. Green; S. Hook; B. Oaida; W. Wu; A. Gunderson; M. Chodas, Global cloud cover for assessment of optical satellite observation opportunities: A HyspIRI case study. Remote Sens. Environ. **2012**, *126*, 62–71.
11. Marco Conoscenti; Riccardo Coppola; Enrico Magli, Constant SNR, Rate Control, and Entropy Coding for Predictive Lossy Hyperspectral Image Compression. IEEE Trans. Geosci. Remote Sens. **2016**, *54*, 7431-7441.
12. Noor. NRM ; Vladimirova. T, Investigation into lossless hyperspectral image compression for satellite remote sensing. International Journal of Remote Sensing. **2013**, *34*, 5072-5104.
13. Nian Yongjian; Xu Ke; Wan Jianwei, Block-based KLT compression for multispectral images. International *J.* of Wavelets Multiresolution and Information Processing. **2016**, *14*.
14. Wang L; Wu JJ; Jiao LC; Shi GM, Lossy-to-Lossless Hyperspectral Image Compression Based on Multiplierless Reversible Integer TDLT/KLT. IEEE Geoscience and Remote Sensing Letters. **2009**, *6*, 587-591.
15. J. Gonzalez-Conejero; J. Bartrina-Rapesta; J. Serra-Sagrista, JPEG 2000 encoding of remote sensing multispectral images with no-data regions. IEEE Geosci. Remote Sens. Lett. **2010**, *7*, 251 – 255.
16. Haoyang Li; Hong Zheng; Chuanzhao Han, Adaptive run-length encoding circuit based on cascaded structure for target region data extraction of remote sensing image. In Proc. International Conference on Integrated Circuits and Microsystems, Chengdu, China, 25-28 November 2016.
17. E. El-Araby; M. Taher; T. El-Ghazawi; J. Le Moigne, Prototyping automatic cloud cover assessment (ACCA) algorithm for remote sensing on-board processing on a reconfigurable computer. IEEE International Conference on Field-Programmable Technology. Singapore, Singapore, 11-14 Dec. 2005.
18. Gao, X.J.; Wan, Y.C.; Zheng, X.Y, Real-Time automatic cloud detection during the process of taking aerial photographs. Spectrosc. Spectr. Anal. **2014**, *34* , 1909–1913.
19. S. A. Ackerman; K. I. Strabala; W. P. Menzel; R. A. Frey; C. C. Moeller; L. E. Gumley, Discriminating clear sky from clouds with MODIS. *J.* Geophys. Res. Atmosp. **1998**, *103*, 32141–32157.
20. S. Ackerman; R. Holz; R. Frey; E. Eloranta; B. Maddux; M. McGill, Cloud detection with MODIS. Part II: Validation. *J.* Atmosp. Ocean. Technol. **1998**, *103*, 1073–1086.

Preprints (www.preprints.org) | NOT PEER-REVIEWED | Posted: 16 November 2017 doi:10.20944/preprints201705.0014.v2

Peer-reviewed version available at Remote Sens. 2018, 10, 152; doi:10.3390/rs10010152

21. R. A. Frey; S. A. Ackerman; Y. Liu; K. I. Strabala; H. Zhang; J. R. Key; X. Wang, Cloud detection with MODIS. Part I: Improvements in the MODIS cloud mask for collection 5. *J.* Atmosp. Ocean. Technol., **2008**, *25*, 1057–1072.
22. Jing Wei; Lin Sun; Chen Jia; Yikun Yang; Xueying Zhou; Ping Gan; Shangfeng Jia; Fangwei Liu; Ruibo Li, Dynamic threshold cloud detection algorithms for MODIS and Landsat 8 data. IEEE International Geoscience and Remote Sensing Symposium, Beijing, China, 10-15 July 2016.
23. M. K. Griffin; H. K. Burke; D. Mandl; J. Miller, Cloud cover detection algorithm for EO-1 hyperion imagery. in Proc. 17th SPIE AeroSense Conf. Algorithms Technol. Multispectral, Hyperspectral Ultraspectral Imagery IX, Orlando, FL, USA, 21-25 July 2003.
24. T. Doggett; R. Greeley; S. Chien; B. Cichy; A. Davies; G. Rabideau; R. Sherwood; D. Tran; V. Baker; J. Dohm; F. Ip, Autonomous on-board detection of cryospheric change with Hyperion on-board Earth Observing-1. in Remote Sens. Environ. **2006**, *101*, 447–462.
25. F. Ip; J. Dohm; V. Baker; T. Doggett; A. Davies; R. Castao; S. Chien; B. Cichy; R. Greeley; R. Sherwood; D. Tran; G. Rabideau, Flood detection and monitoring with the autonomous sciencecraft experiment onboard EO-1. Remote Sens. Environ. **2006**, *101*, 463–481.
26. Richard R. Irish., Landsat 7 automatic cloud cover assessment. Algorithms for Multispectral, Hyperspectral, and Ultraspectral Imagery, Proceedings of SPIE, Orlando, FL USA, 24, April, 2000.
27. M. Wang; W. Shi, Cloud masking for ocean color data processing in the coastal regions. IEEE Trans. Geosci. Remote Sens. **2006**, *44*, 3105–3196.
28. Juan Deng, Hongchen Wang, Jun Ma, An Automatic cloud detection algorithm for Landsat Remote Sensing Image. 4th International Workshop on Earth Observation and Remote Sensing Applications, Guangdong, China, 11-14 Dec. 2016.
29. L. Gómez-Chova; G. Camps-Valls; J. Calpe-Maravilla; L. Guanter; J. Moreno, Cloud-screening algorithm for ENVISAT/MERIS multispectral images. IEEE Trans. Geosci. Remote Sens., **2007**, *45*, 4105–4118.
30. T. Taylor; C. O'Dell; D. O'Brien; N. Kikuchi; T. Yokota; T. Nakajima; H. Ishida; D. Crisp; T. Nakajima, Comparison of cloud-screening methods applied to GOSAT near-infrared spectra. IEEE Trans. Geosci. Remote Sens., **2012**, *50*, 295–309.
31. P. Minnis; Q. Z. Trepte; S. Sun-Mack; Y. Chen; D. R. Doelling; D. F. Young; D. A. Spangenberg; W. F. Miller; B. A. Wielicki; R. R. Brown; S. C. Gibson; E. B. Geier, Cloud detection in nonpolar regions for CERES using TRMM VIRS and terra and aqua MODIS data. IEEE Trans. Geosci. Remote Sens., **2008**, *46*, 3857–3884.
32. J. Lee; R.Weger; S. Sengupta; R.Welch, A neural network approach to cloud classification. IEEE Trans. Geosci. Remote Sens., **1990**, *28*, 846–855.
33. J. V. Martins; D. Tanré; L. Remer; Y. Kaufman; S. Mattoo; R. Levy, MODIS cloud screening for remote sensing of aerosols over oceans using spatial variability. Geophys. Res. Lett., **2002**, *29*, MOD4-1–MOD4-4.
34. Jinhu Bian; Ainong Li; Qiannan Liu; Chengquan Huang, Cloud and Snow Discrimination for CCD Images of HJ-1A/B Constellation Based on Spectral Signature and Spatio-Temporal Context. Remote Sensing, **2016**, *8*, 1-31.
35. F. Murtagh, D. Barreto, and J. Marcello, Decision boundaries using Bayes factors. IEEE Trans. Geosci. Remote Sens., **2003**, *41*, 2952–2958.
36. Haoyang Yu; Lianru Gao; Jun Li; Shansan Li; Bing Zhang, Spectral-Spatial Hyperspectral Image Classification Using Subspace-Based Support Vector Machines and Adaptive Markov Random Fields. Remote Sensing., **2016**, *8*, 1-21.
37. C. Merchant, A. Harris, E. Maturi, and S. MacCallum, Probabilistic physically based cloud screening of satellite infrared imagery for operational sea surface temperature retrieval. Q. J. R. Meteorol. Soc., **2005**, *131*, 2735–2755.
38. David R. Thompson; Robert O. Green; Didier Keymeulen; Sarah K. Lundeen; Yasha Mouradi; Daniel Cahn Nunes; Rebecca Castaño; Steve A. Chien, Rapid Spectral Cloud Screening Onboard Aircraft and Spacecraft. IEEE Trans. on Geosci. and Remote Sens., **2014**, *52*, 6779 - 6792.
39. Li Wei; Wu Guodong; Zhang Fan; Qian Du, Hyperspectral Image Classification Using Deep Pixel-Pair Features. IEEE Trans. on Geosci. and Remote Sens., **2017**, *55*, 645-657.
40. Bin Pan; Zhenwei Shi; Xia Xu, R-VCANet: A New Deep-Learning-Based Hyperspectral Image Classification Method. IEEE Journal of Selected Topics in Applied Earth Observations and Remote Sensing, **2017**, *10* , 1975 – 1986.

Preprints (www.preprints.org) | NOT PEER-REVIEWED | Posted: 16 November 2017 doi:10.20944/preprints201705.0014.v2

Peer-reviewed version available at Remote Sens. 2018, 10, 152; doi:10.3390/rs10010152

41. Pasquale L. Scaramuzza; Michelle A. Bouchard; John L. Dwyer, Development of the Landsat Data Continuity Mission Cloud-Cover Assessment Algorithms. IEEE Trans. on Geosci. and Remote Sens. **2012**, *50* , 1140-1157.
42. Liu, J., Improvement of dynamic threshold value extraction technic in FY-2 cloud detection. *J.* Infrared Millim. Waves. **2010**, *29* , 288–292.
43. Haoyang Yu, Lianru Gao, Jun Li, Shan Shan Li, Bing Zhang and Jón Atli Benediktsson, Spectral-Spatial Hyperspectral Image Classification Using Subspace-Based Support Vector Machines and Adaptive Markov Random Fields. Remote Sensing. **2016**, *8* , 1-21.
44. Tarabalka, Y.; Benediktsson, J.A.; Chanussot, J., Spectral-spatial classification of hyperspectral imagery based on partitional clustering techniques. IEEE Trans. Geosci. Remote Sens. **2009**, *47* , 2973–2987.
45. Hu Haifeng; Zhao Jianping; Wu Dongmei; Lu Na; Qin Yongyi, Implementation of Arccosine Function Based on FPGA. Electronic Technology. **2013**, *6* , 5-8.
46. Tang Wen-ming, Liu Gui-xiong, FPGA Fixed-Point Technology of Exponential Function Achieved by CORDIC Algorithm. *J.* of South China University of Technology(Natural Science Edition), **2016**, *44*, 9-14.
47. Peter Malík, High throughput floating point exponential function implemented in FPGA. IEEE Computer Society Annual Symposium on VLSI, Montpellier, France, 08 - 10 Jul 2015.
48. Wolfram Hergert; Thomas Wriedt, The Mie Theory. Springer Series in Optical Sciences, **2012**,*169*.
49. Yang, P.; L. Bi; B. A. Baum; K. N. Liou; G. W. Kattawar; M. Mishchenko and B. Cole, Spectrally consistent scattering, absorption, and polarization properties of atmospheric ice crystals at wavelengths from 0.2 to 100 μm. *J.* Atmos. Sci., **2013**, *70*, 330-347.